Available online at www.sciencedirect.com

SCIENCE DIRECT®

Journal of Controlled Release 107 (2005) 112–121

journal of controlled release

www.elsevier.com/locate/jconrel

On the study of BSA-loaded calcium-deficient hydroxyapatite nano-carriers for controlled drug delivery

Tse-Ying Liu [a], San-Yuan Chen [a,*], Dean-Mo Liu [b], Sz-Chian Liou [c]

[a] *Department of Materials Science and Engineering, National Chiao Tung University 1001 Ta-hsueh Rd., Hsinchu, Taiwan, ROC*
[b] *ApaMatrix Technologies Inc. 58-7151 Moffatt Road, Richmond, British Columbia, Canada V6Y3G9*
[c] *Department of Advanced Failure Analysis Service, Advanced Product Engineering Division, Taiwan Semiconductor Manufacturing Company, 6 Creation Rd. 2, Hsinchu, Taiwan, ROC*

Received 7 September 2004; accepted 24 May 2005
Available online 27 June 2005

Abstract

Calcium-deficient hydroxyapatite (CDHA) nano-crystals incorporated with bovine serum albumin (BSA) to form BSA-loaded nano-carriers were synthesized via both in-situ and ex-situ processes. Amount of BSA uptake by the CDHA nano-crystals and subsequent release behaviors of the BSA-loaded nano-carriers were investigated. The amount of BSA uptake by CDHA decreases with increasing pH but a larger amount was observed in the ex-situ compared to in-situ process above pH = 8.0. The release profile showed a bursting behavior for the nano-carrier prepared via the ex-situ process, which is probably due to the desorption of BSA molecules. In contrast, for the sample synthesized via the in-situ process at a higher pH level, a slower release profile without bursting behavior due to the dissolution of the BSA-incorporated CDHA crystal is seen from high solution TEM that indicates different extent of interaction between BSA and CDHA. On the other hand, for the nano-carriers prepared via the same process at lower pH level, a two-stage release profile was detected. An initial bursting release is due to the desorption of BSA from the CDHA surface, followed by a slow release as a result of the dissolution of the BSA-incorporated nano-crystals along its *c*-axis direction.

Keywords: Nano-carrier; Aspect ratio; In-situ process; Calcium-deficient hydroxyapatite; BSA; Release behaviors

1. Introduction

Hydroxyapatite (HA), having a chemical formula $Ca_{10}(PO_4)_6(OH)_2$, is a naturally occurring inorganic material that has been a mineralized tissue of bones and teeth in humans and vertebrates. HA has been well-recognized as it is an excellent biocompatible and bioactive material for a number of clinical demands in the areas of orthopedics and dentistry for the past several decades. The use of HA as adsorbent for biomolecules has also attracted a great deal of attention over the years, because HA has long been

* Corresponding author. Tel.: +886 3 5731818; fax: +886 3 5725490.
E-mail address: sychen@cc.nctu.edu.tw (S.-Y. Chen).

0168-3659/$ - see front matter © 2005 Elsevier B.V. All rights reserved.
doi:10.1016/j.jconrel.2005.05.025

recognized as having excellent affinity to biological substances, such as collagen, proteins, enzymes, cells, and viruses [1,2].

Incorporation of active agents or drugs by physical absorption within porous HA-based implants has been frequently reported for orthopedic uses [3–5]. However, low efficiency of drug encapsulation due to limited surface area has remained an issue to be resolved. On the other hand, the inconsistency of therapeutical effect of different drugs may encounter when a multiple drug administration is operated, whereas sequential release and simultaneous release of multiple drugs are hardly properly controlled by the same carrier to, for instance, enhance osteogenesis and suppress antibiotic resistance, respectively [6–8]. These drawbacks seem to be easily overcome by the use of micro-carriers or nano-carriers delivering antibiotics and growth factors with controlled release kinetics regulated by different synthetic process. Ijntema et al. employed HA microcrystals as micro-carriers to load BSA of 5–10 wt.% and concluded that it would be a step ahead if the apatitic crystals are able to carry higher amount of the active agents for a variety of biomedical purposes such as drug delivery, orthopedics and dentistry [9]. Furthermore, it is particularly critical for those areas where a higher dosage of drugs with relatively small amount of the carrier is required.

Very recently, there has been growing interest in nano-crystals as carriers for bioactive agents. Ueno et al. employed nano-sized $CaCO_3$ as carrier for sustain release of betamethasone phosphate [10]. Matsumoto et al. investigated the influence of protein concentration and synthetic temperature on the protein release from HA nano-carrier [11]. However, studies on the release mechanism of protein-loaded nano-carriers through the manipulation of synthesis are rarely found in the literature but very important.

The apatite crystal often used to carry drugs or proteins has regularly a stoichiometric composition, i.e., Ca/P = 1.67, in the literature. However, mineralized apatite in humans and vertebrates is essentially non-stoichiometric, i.e., Ca/P < 1.67, or more specifically, a calcium-deficient hydroxyapatite, i.e., CDHA. Therefore, it is technically important to simulate the synthesis of CDHA nano-crystals in the presence of active agent. As the main concern of this communication, BSA was employed as a model protein to further understand the loading efficiency and release behavior of the BSA in CDHA nano-carriers. Therefore, the influences of synthetic solution pH and processing variation on the incorporation of BSA molecules with CDHA were systematically investigated. In addition, in order to gain better understanding on the interfacial structure between BSA and CDHA, nano-structure at BSA–CDHA interface was further explored by high resolution transmission electron microscopy (HR-TEM) and electron energy loss spectroscopy (EELS). The subsequent release behaviors of the resulting BSA-loaded CDHA nano-particles were explored and correlated with the synthesis scheme proposed in this investigation.

2. Materials and methods

2.1. BSA-loaded CDHA synthesis

0.25 M $Ca(CH_3COO)_2$ solution and 0.16 M H_3PO_4 solution were used as precursors of Ca and P to prepare CDHA nano-particles, respectively. The molar ratios of Ca to P were fixed at 1.5 and bovine serum albumin (BSA, Aldrich, A-7638) was selected as candidate protein in this study. A BSA aqueous solution of 1500 μg/ml was prepared by dissolving BSA powder into distilled water for each synthesis process. For in-situ synthetic process A, BSA solution was dropped into H_3PO_4 solution maintained at pH 7.5, pH 8.5 and pH 9.5 by the addition of NaOH solution (1 M) and the samples were named as A-7.5, A-8.5 and A-9.5, respectively (see Table 1). Subsequently, $Ca(CH_3COO)_2$ solution was dropwisely added into the above solution to form suspensions.

Table 1
Synthetic conditions of the BSA–CDHA nano-carriers

Process	Adding sequence	pH range	Sample name
In-situ process A	$H_3PO_4 \rightarrow BSA \rightarrow Ca(CH_3COO)_2$	7.5	A-7.5
		8.5	A-8.5
		9.5	A-9.5
In-situ process B	$Ca(CH_3COO)_2 \rightarrow BSA \rightarrow H_3PO_4$	7.5	B-7.5
		8.5	B-8.5
		9.5	B-9.5
Ex-situ process C	$CDHA \rightarrow BSA$	7.5	C-7.5
		8.5	C-8.5
		9.5	C-9.5

On the other hand, in order to understand the importance of synthesis sequence on the BSA-loaded CDHA nano-particles, BSA solution was first mixed with $Ca(CH_3COO)_2$ solution instead of H_3PO_4. After that, H_3PO_4 was added into the solution to form suspensions. The samples were named as B-7.5, B-8.5 and B-9.5. For comparison, ex-situ synthetic process was also prepared. CDHA powder was first prepared at pH 7.5 and dispersed in DI water. The obtained suspension was then mixed with the BSA solution in the range of pH from 7.5 to 9.5, namely as sample C-7.5, C-8.5 and C-9.5. For all the synthetic processes, the suspensions were filtered off and the resulting precipitates were then washed with phosphate-buffered solution (PBS buffered with HCl at pH 6.8) and DI water for 3 times for further characterization.

2.2. Characterization

The relative amount of the BSA associated with the CDHA nano-particles was determined using thermogravimetric analysis, TGA (Perkin Elmer), with a heating rate of 10 °C/min. Crystallographic phase of the BSA-loaded CDHA powders was identified by X-ray diffractometer (M18XHF, Mac Science, Tokyo, Japan), at a scanning rate of 4° 2θ per min over a range of 2θ from 20° to 60°. Fourier transform Infrared (FT-IR) spectra were recorded on a spectrometer (Model 580, Perkin-Elmer) using a compressed pellet of about 1 mm thick prepared by a mixture of 100 mg of KBr and 1 mg of the BSA powders. The FT-IR spectra were taken with a resolution of 4.00 cm^{-1} in the range of 4000–400 cm^{-1} and were averaged from 128 scans. Microstructure observations were performed using a Philips Tecnai 20 (Holland, The Netherlands) transmission electron microscope operated at 200 keV and equipped with a Gatan image filter (GIF, Model GIF-2000) for EELS analysis. EELS spectra were obtained with an energy resolution of 1 eV (zero-loss peak) and an energy dispersion of 0.2 eV per channel.

2.3. Release test

Bovine serum albumin-loaded CDHA nano-particles (0.15 g) were dispersed in 10 ml buffer solution buffered with NaOH and $C_6H_8O_7$ at pH 6 with a stirring rate of 100 rpm at 37 °C. The BSA release test was carried out by taking 0.1 ml of the buffer solution and 2 ml of bicinchoninic acid solution (Sigma, bicinchoninic acid protein assay kit, BCA-1 and B9643) for each juncture. UV–visible spectroscopy (Agelent 8453) was used for the characterization of absorbance peaks at 562 nm to determine the BSA concentration through the use of a pre-determined standard concentration–intensity calibration curve.

3. Results and discussion

3.1. Material characterization

Fig. 1 shows the FT-IR spectra of the BSA-loaded nano-particles. The IR spectra of pure BSA and CDHA are also shown for comparison. The spectrum of BSA exhibited an apparent absorption band at 1654 cm^{-1} assigned to amide I, C=O stretching mode, 1540 cm^{-1} assigned to amide II, N–H bending mode and 1384 cm^{-1} assigned to amide III, C–N stretching mode and N–H bending mode. The spectrum of the pure CDHA presents the characteristic absorption band at 1640 cm^{-1} assigned to molecular water, 1092 and 1040 cm^{-1} assigned to P–O stretching mode, and 602 cm^{-1} and 563 cm^{-1} assigned to O–P–O bending mode. For in-situ process (A, B), the band at 1652 cm^{-1} was likely due to the overlap of 1654 cm^{-1} and 1640 cm^{-1}, suggesting that all the CDHA powders are associated with BSA. These

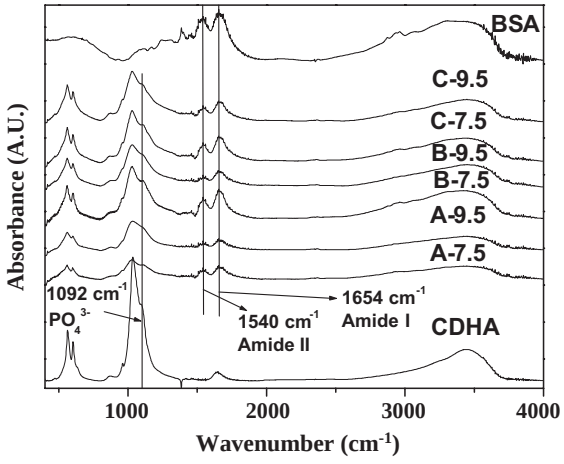

Fig. 1. FT-IR spectra of the nano-carriers synthesized in different conditions.

broad, featureless v_3 PO_4^{3-} bands at 1092–1040 cm^{-1} in both samples of A-9.5 and B-9.5 also suggest that the resulting crystals exhibit poorly-crystalline structure. It was noted that for all synthetic conditions, no significant red shift of carboxylate band (1338 cm^{-1}) was detected in the final CDHA–BSA composite powders, indicating no chemical bonding between surface Ca^{2+} of the CDHA and COO^- (BSA) was observed in the BSA-loaded CDHA powder [12].

Three possible mechanisms can be adapted to explain the interaction between the CDHA and BSA molecules. The first mechanism can be of Ca-bridging: This charge-transfer bonding was reported by Ellingsen [13], considering that acid proteins bind to the P-sites of the HA particles through O^-Ca^{2+}–COO^- (Ca-bridging). The P-site is a negatively-charged site formed by six oxygen atoms of phosphate of the *ab* crystal plane of the HA [14]. Similar behavior can be applied to the CDHA nano-crystals currently synthesized. The second one can be operated through the electrostatic interaction between the positive Ca^{2+} and COO^- (BSA): this has been also reported by Liou et al. [15] who suggested that there is an intermediate complex between COO^- and CDHA. This complex can be formed via the electrostatic interaction between the negative COO^- on BSA molecule and positive Ca^{2+} on the C-sites of CDHA surface. Kandori et al. [14] indicated that the C-sites were located on the crystal planes that are perpendicular to *a*-axis and *b*-axis of apatite crystal. These C-sites were developed as a result of the calcium ions on the CDHA surface, thus making positive charges to attract COO^- groups of BSA molecules. The third one is based on the formation of acetate salt which is an intermediate product between calcium ions and COO^- (BSA) after synthesis, or more specifically, a BSA-bonding Ca ion. However, both Ca-bridging and BSA-bonding Ca ions cannot further react with $(PO_4)^{3-}$ and/or $(HPO_4)^{2-}$ to form CDHA nano-crystals in the solution. Therefore, once it (Ca-bridging and/or BSA-bonding Ca ions) occurred, a lower production yield of CDHA formation than those predesigned (theoretical) can be observed. This is further evidenced in Fig. 2, where about 15% of the Ca ions were associated with the BSA, thus a CDHA production yield ratio (i.e., the ratio of real to theoretical production yield) of 85% was attained at the $Ca(CH_3COO)_2$ concentration of 0.25 M (i.e., the corresponding ratio of Ca^{2+} to amino acid residue was calculated as 3.16 and shown in the second *Y*-axis of Fig. 2). As the concentration of $Ca(CH_3COO)_2$ was further decreased (i.e., the corresponding ratio of Ca^{2+} to amino acid residue was decreased), a decreased CDHA yield ratio was observed. This suggests that an interaction takes place between the BSA molecules and Ca ions via Ca-bridging or BSA-bonding Ca ions. However, as mentioned before, no red shift of carboxylate band at 1338 cm^{-1} was observed for all BSA-loaded CDHA samples. Therefore, it is inferred that Ca-bridging plays an important role between BSA molecules and CDHA crystals.

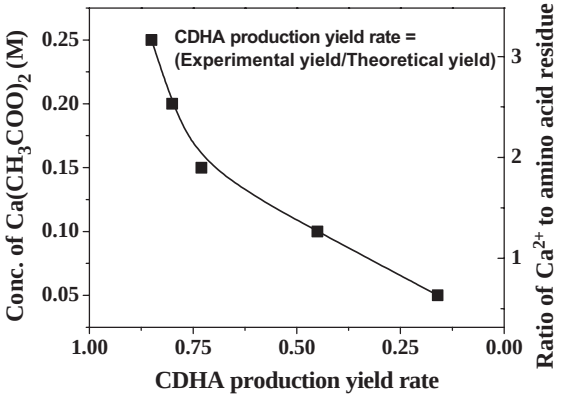

Fig. 2. Dependence of $Ca(CH_3COO)_2$ concentrations on the CDHA production yield rate. The corresponding ratio of Ca^{2+} to amino acid residue was calculated and shown in the second *Y*-axis.

Fig. 3 shows the X-ray diffraction (XRD) patterns of the BSA-loaded CDHA nano-powders. Two major characteristic diffraction peaks could be obtained for all the powdered samples: one closed at 2θ of ~26° and the other broad one at ~32°. According to ICDD No. 46-0905, it can be indexed as a poorly crystalline calcium-deficient apatite structure. No considerable difference in those characteristic diffraction peaks was discerned for both synthetic sequences outlined above. This may suggest that the presence of the BSA during the synthesis of the CDHA does not give pronounced influence on the structural development of the CDHA nano-crystals.

3.2. BSA incorporation with CDHA

Fig. 4a shows the HR-TEM nano-structure of sample B-9.5 (in-situ process) and corresponding

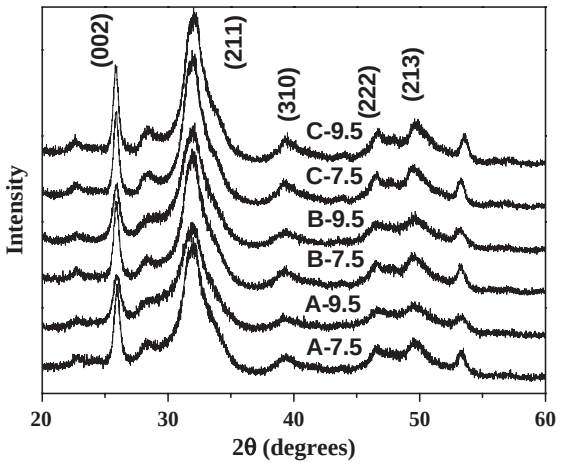

Fig. 3. XRD patterns of the BSA-loaded CDHA nano-carriers synthesized in different conditions.

color-enhanced image is illustrated in Fig. 4b. As it can be seen, the nano-structure of the BSA–CDHA hybrid may be divided into 4 regions as indicated with different colors. In region A, the lattice fringes parallel to (100) CDHA were clearly observed in the long needle-like crystallites, indicating a well-crystallized region. Region B, i.e., the layer nearest to the highly crystalline inner layer, is formed with a lattice development strongly affected by the nearest region of highly-order structure. Region B is a result of "growth inhibition". In other words, much poor crystallization was observed [16]. As the crystal continuously grows, the effect of BSA molecule becomes stronger in distributing the deposition of Ca-P materials, and in a certain case, conjugate as a complex and integrate into "outer area of the lattice" (the so-called BSA–CDHA complex), resulting in an amorphous region C. However, from its nano-structure, the crystallization is prohibited, and this may be caused by, possibly, a regulation of lattice mismatch resulting in somewhat "gradient crystallinity". The outer region D can be considered as a transition region from BSA–CDHA complex to absorption BSA. An adsorbed BSA layer is essentially tangled with the underlying CDHA–BSA complex (region C).

It was also found that both nano-sized CDHA crystal and BSA-loaded CDHA samples prepared via the ex-situ process were more susceptible to electronic beam bombardment than that prepared via in-situ process, thus causing radiolysis under HR-TEM analysis [17]. This probably reveals that different extent of interaction exists between CDHA and BSA for in-situ and ex-situ processes, which could be further explored via derivative thermogravimetry (DTG) analysis as shown in Fig. 5. For in-situ processes of A-9.5 and B-9.5, a broad band at 400 °C were detected, which is probably attributed to the thermal decomposition of the BSA–CDHA complex. Due to the incorporation of BSA molecules into regions C and D through electrostatic force (C sites) and/or Ca-bridging (P-sites), a higher thermal decomposition temperature was observed for BSA–CDHA complex compared to that of pristine BSA (350 °C). For the sample prepared in a lower pH value (A-7.5 and B-7.5), this band at 400 °C was not only detected

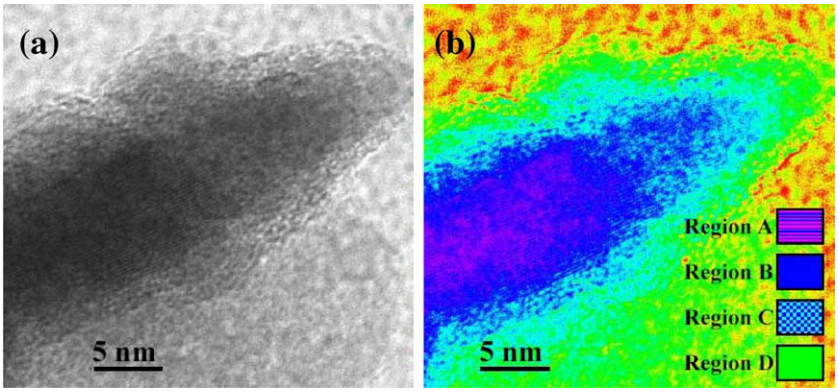

Fig. 4. (a) HR-TEM photograph of the BSA-loaded CDHA nano-carriers prepared through in-situ processes at pH=9.5, (b) corresponding color-enhanced image of (a).

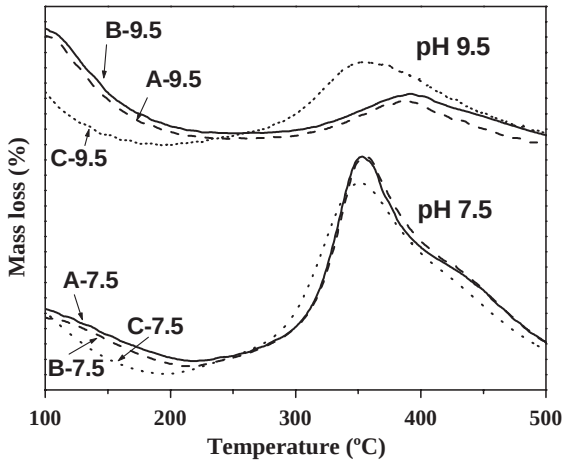

Fig. 5. DTG curves of the BSA-loaded CDHA nano-carriers synthesized in different conditions.

but also the other strong band at 350 °C was detected. The latter band can be primarily attributed to the thermal decomposition of adsorbed BSA molecules. The adsorption of BSA onto CDHA nano-crystals can be considered as a type of pseudo-Langmuir adsorption [14]. In other words, a number of the BSA layers are adsorbed on CDHA surface which are not tightly bound with CDHA crystals. Therefore, thermal decomposition temperature of adsorbed BSA molecule is close to that of pristine BSA. However, the band at 350 °C was not detected for both samples of A-9.5 and B-9.5, which is probably due to the fact that the outer-layered BSA molecules are easily eluted in the solution with a higher pH value upon synthesis [1]. In contrast, for the samples prepared via ex-situ processes, only a band at 350 °C was observed. This reflects that no strong interaction exists in the interface of the BSA molecules and CDHA crystals for the samples prepared via ex-situ process.

The TEM images in Fig. 6a–c show that the BSA-loaded CDHA nano-crystals synthesized in different conditions present needle-like morphology with dimensions of 4–12 nm in diameter and 40–70 nm in length. The particle size was measured from the TEM images and each datum was averaged from at least 10 TEM photographs. Furthermore, it was ob-

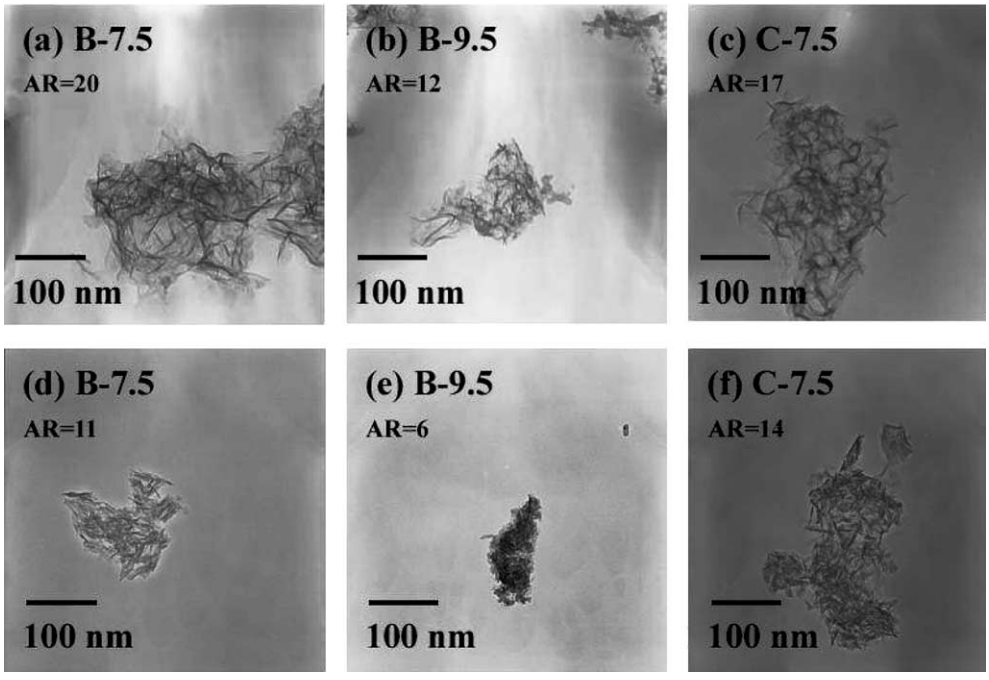

Fig. 6. TEM micrographs of the BSA-loaded CDHA nano-carriers prepared through different processes, (a)–(c) showing the effect of processing variation on morphology and size of CDHA nano-crystals before release test, (d)–(f) showing a further reduction in both aspect ratio and size of the CDHA nano-crystals after release test compared to that before the test. The aspect ratios were measured from the TEM images and each datum was averaged from at least 10 TEM photographs.

served that crystal morphology was changed with an increase of solution pH for the in-situ processes (A and B). The dependence of the solution pH value on the aspect ratio of CDHA nano-crystals is further illustrated in Fig. 7a. It is interesting to note that the resulting BSA-loaded CDHA nano-crystals derived from the higher pH solution (A-9.5 and B-9.5) showed a smaller aspect ratio compared to that synthesized at a lower pH solution (A-7.5 and B-7.5). Such a preferential growth in the solution at a lower pH can be correlated with preferential adsorption. It means that more BSA should be adsorbed onto the C-sites of the CDHA nano-crystals at a lower pH value, which causes considerable preferential inhibition effect on the growth of nano-crystals along the *ab* axis, resulting in a high aspect ratio [18]. In contrast, at a higher solution pH, $O^{-}Ca^{2+}$–COO^{-} (Ca-bridging) is prominent due to the stability of $(PO_4)_3^{-}$. Therefore, crystal growth of both C-sites and P-sites are inhibited, resulting in a lower aspect ratio. Moreover, it is known that the conformation of protein could be more linear (unfolding) in the solution with strong base and ionic strength [19]. The resulting unfolding BSA molecules and/or amino acid residues strongly attracted Ca^{2+} through the formation of Ca-bridging [20], which kinetically lead to the inhibition growth on the P-sites of CDHA crystals at the earlier crystallization stage. Therefore, the aspect ratio for nano-carriers prepared via the in-situ process at higher pH is reduced.

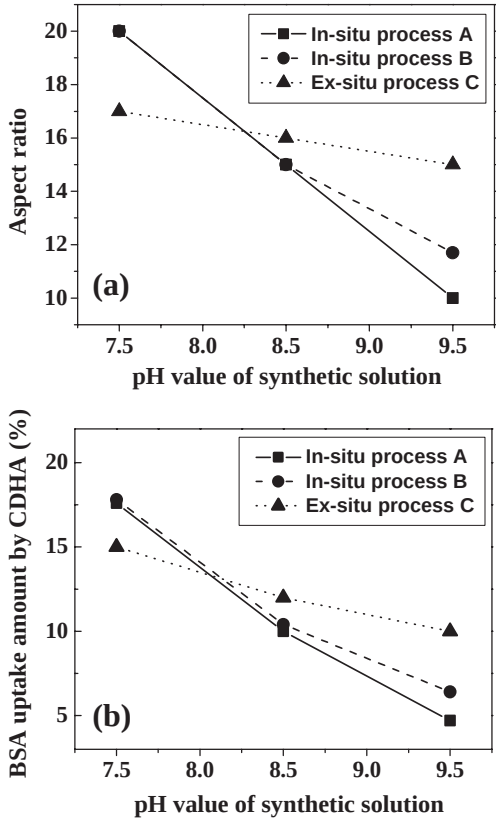

Fig. 7. Dependence of the pH value of synthetic solution on the (a) aspect ratio of CDHA crystal, (b) amount of BSA uptake by CDHA nano-crystal.

The corresponding amount of the BSA uptake by the CDHA particles (after calibration by subtracting water content) determined from the TGA is shown in Fig. 7b. Obviously, a lower pH resulted in a higher BSA incorporation, and as high as 17.5 wt.% of the BSA associated with the CDHA was detected, which is about 75% higher than that reported in the literature [9]. In contrast, since the isoelectric point (IEP) of CDHA and BSA is around 7 and 4.7, respectively [21,22]. It is then expected that the electrostatic repulsive force between the BSA and CDHA nano-crystal becomes dominant for a solution with a higher pH (9.5) compared to that with a lower pH (7.5). Therefore, an increase in solution pH resulted in a decreased amount of BSA.

Considerable differences in the amount of the BSA uptake associated with the CDHA at pH 9.5 can be seen from Fig. 7b, where the CDHA carries a higher amount of the BSA from the ex-situ process (C-9.5) than that from the in-situ processes (A-9.5 and B-9.5). This may be explained by the aspect ratio of the CDHA carries, as illustrated in Fig. 7a which showed the aspect ratio of the nano-carriers prepared via the ex-situ process (C-9.5) was higher than that prepared via the in-situ process (A-9.5, B-9.5). The CDHA nano-particles with a higher aspect ratio indicates a higher population of the positively-charged C-sites for BSA adsorption and therefore, the total effective areas of adsorption sites (C-site) are much larger for the high aspect-ratio nano-particles compared to that of low aspect-ratio nano-particles per unit weight. If the above argument is correct, then, it is conceivable to realize that the ex-situ CDHA carries higher amount of the BSA than those in-situ CDHA at pH 9.5. However, at pH 7.5, the preferential growth along *c*-axis for carriers prepared via in-situ process (A-7.5, B-

7.5) resulted in a larger aspect ratio compared to that prepared via ex-situ process (C-7.5). Consequently, in contrast to that at pH 9.5, a higher amount of BSA (about 10 wt.%) was detected in the in-situ CDHA than the ex-situ CDHA at pH 7.5.

3.3. Controlled BSA release

The BSA release profiles of the BSA-loaded CDHA nano-crystals are shown in Fig. 8. It was found that samples prepared from ex-situ processes (C-7.5 and C-9.5) showed a pronounced bursting behavior for the initial time period of 8 h during which BSA were nearly entirely released. The bursting release of BSA can be assigned to the desorption of BSA molecules which are not tightly bound with CDHA surface. In contrast, although the BSA-loaded CDHA nano-crystals prepared from the in-situ processes (A-7.5, B-7.5) showed bursting release behaviors in the initial time period, a slow release was then followed, suggesting a two-stage release mechanism. The BSA release behavior in the initial stage is similar to that of the samples prepared from ex-situ process. This busting release could be assigned to the desorption of BSA molecules which were not strong interacted with CDHA crystals. The release profile in the second stage may be attributed to the BSA molecules which have been incorporated into CDHA crystals (BSA–CDHA complex). This slow release may result from the dissolution of CDHA crystal, which will be

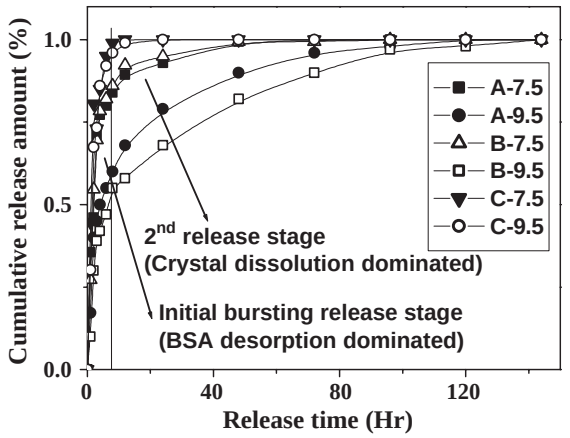

Fig. 8. BSA release profiles of the BSA-loaded CDHA nano-carriers synthesized in different conditions.

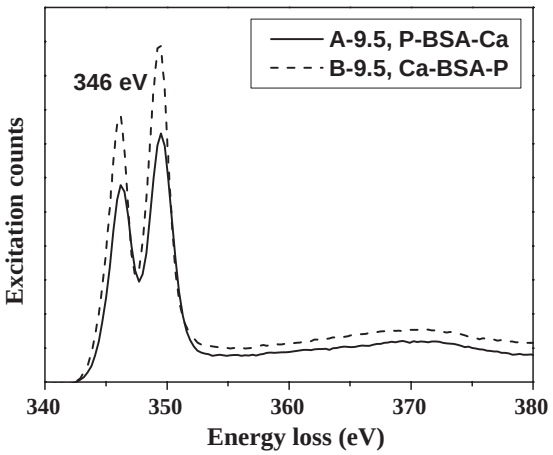

Fig. 9. ELNES spectra near the Ca $L_{2,3}$-edge of BSA-loaded CDHA nano-carriers prepared through in-situ processes at pH = 9.5.

further discussed later. However, as the BSA-loaded CDHA nano-crystal was prepared from in-situ process with a higher solution pH value (A-9.5 and B-9.5), only a single-stage slow release profile was detected, which may be also attributed to the release of incorporated BSA from BSA–CDHA complex.

Moreover, as shown in Fig. 6, it was found that a considerable reduction in the dimension of *c*-axis was observed after release test for particularly the CDHA nano-crystals prepared via in-situ process. This observed size reduction may suggest that the dissolution of the CDHA nano-crystals is highly anisotropic with respect to the crystal plane of the CDHA particles. This result is further supported by HR-TEM shown in Fig. 4b, where P-sites were rich in amorphous region C causing higher *c*-axis dissolution rate compared to both *a* and *b* axes. If the above argument is correct, it is conceivable to realize that crystal dissolution in *c*-axis is responsible for the slow release of incorporated BSA from BSA–CDHA complex [16]. Moreover, in order to explore the difference in the release profiles between samples A-9.5 and B-9.5, electron energy loss spectroscopy (EELS) was employed to explain subtle variation in the local structure of nano-scale regions. As shown in Fig. 9, the excitation counts of Ca $L_{2,3}$-edges with energy-loss ranging from 340 to 360 eV were smaller for A-9.5 than those for B-9.5. According to the Fermi golden rule of quantum mechanics [23], a structural disorder presents a lower excitation count peak in electron-energy loss near-

edge structure (ELNES). This may suggest that the crystallinity of A-9.5 is poorer than that of B-9.5, which subsequently results in the higher release (also dissolution) rate of sample A-9.5.

It can then be concluded that the release profile was first dominated by BSA desorption, followed by a slow release controlled by crystal dissolution. Although the nature of the interaction between BSA and CDAH is not fully understood at present, this study suggests that the resulting release profile permits a design of the CDHA nano-crystal as nano-carrier for drug release.

4. Conclusion

In summary, the amount of BSA uptake was dependent on the solution pH and processing variation, i.e., in-situ and ex-situ synthetic schemes. Moreover, both synthetic process and pH value upon synthesis significantly altered the drug release behaviors of BSA-loaded CDHA nano-carriers. It is feasible to employ the CDHA nano-carrier to load protein, such as acid growth factor and acid protein-drug conjugation, as component of bone substitutes or as a reinforced filler together with a pre-designed drug release function for particular therapeutic effect.

Acknowledgement

The authors gratefully acknowledge the National Science Council of the Republic of China for its financial support through Contract No. NSC-92-2216-E-009-025. The authors would also like to thank ApaMatrix Technologies Inc., Canada, for technical support.

References

[1] M.J. Gorbunoff, The interaction of proteins with hydroxyapatite, Anal. Biochem. 136 (1984) 425–432.
[2] A. Barroug, M.J. Glimcher, Hydroxyapatite crystals as a local delivery system for cisplatin: adsorption and release of cisplatin in vitro, J. Orthopaed. Res. 20 (2002) 274–280.
[3] G. Goller, F.N. Oktar, Sintering effects on mechanical properties of biologically derived dentine hydroxyapatite, Mater. Lett. 56 (2002) 142–147.
[4] J.A. Koempel, B.S. Patt, K. O'Grady, J. Wozney, D.M. Toriumi1, The effect of recombinant human bone morphogenetic protein-2 on the integration of porous hydroxyapatite implants with bone the amount of bone growth into the implant, J. Biomed. Mater. Res. 41 (1998) 359–363.
[5] M.B Yaylaoglu, P. Korkusuz, Ü. Örs, F. Korkusuz, V. Hasirci, Development of a calcium phosphate–gelatin composite as a bone substitute and its use in drug release, Biomaterials 20 (1999) 711–719.
[6] A.T. Raiche, D.A. Puleo, In vitro effects of combined and sequential delivery of two bone growth factors, Biomaterials 25 (2004) 677–685.
[7] M. Tatman-Otkun, S. Gurcan, B. Ozer, N. Shokrylanbaran, Annual trends in antibiotic resistance of nosocomial *Acinetobacter baumannii* strains and the effect of synergistic antibiotic combinations, Microbiologica 27 (2004) 21–28.
[8] Y.W. Miller, E.A. Eady, R.W. Lacey, J.H. Cove, D.N. Joanes, W.J. Cunliffe, Sequential antibiotic therapy for acne promotes the carriage of resistant staphylococci on the skin of contacts, J. Antimicrob. Chemother. 38 (1996) 829–837.
[9] K.I. Jntema, W.J.M. Heuvelsland, C.A.M.C. Dirix, A.P. Sam, HA microcarriers for biocontrolled release of protein drugs, Int. J. Pharm. 112 (1994) 215–224.
[10] Y. Ueno, H. Futagawa, Y. Takagi, A. Ueno, Y. Mizushim, Drug-incorporating calcium carbonate nanoparticles for a new delivery system, J. Control. Release 103 (2005) 93–98.
[11] T. Matsumotoa, M. Okazakib, M. Inouec, S. Yamaguchic, T. Kusunosec, T. Toyonagaa, Y. Hamadaa, J. Takahashi, Hydroxyapatite particles as a controlled release carrier of protein, Biomaterials 25 (2004) 3807–3812.
[12] Sang-Hoon Rhee, Jae-Do Lee, Nucleation of hydroxyapatite crystal through chemical interaction with collagen, J. Am. Ceram. Soc. 83 (2000) 2890–2892.
[13] J.E. Ellingsen, A study on the mechanism of protein adsorption to TiO_2, Biomaterials 12 (1991) 593–596.
[14] K. Kandori, M. Saito, H. Saito, A. Yasukawa, T. Ishikawa, Adsorption of protein on non-stoichiometric calcium–strontium hydroxyapatite, Colloids Surf., A Physicochem. Eng. Asp. 94 (1995) 225–230.
[15] S.C. Liou, S.Y. Chen, D.M. Liu, Synthesis and characterization of needlelike apatitic nanocomposite with controlled aspect ratios, Biomaterials 24 (2003) 3981–3988.
[16] T. Matsumoto, M. Okazaki, M. Inoue, Y. Hamada, M. Taira, J. Takahashi, Crystallinity and solubility characteristics of hydroxyapatite adsorbed amino acid, Biomaterials 23 (2002) 2241–2247.
[17] S. Nicolopoulos, J.M. Gonza'lez-Calbet, M.P. Alonso, M.T. Gutierrez-Rios, M.I. de Frutos, M. Vallet-Regi, Characterization by TEM of local crystalline changes during irradiation damage of hydroxyapatite compounds, J. Solid State Chem. 116 (1995) 265–274.
[18] V. Hlady, H. Furedi-Milhofer, Absorption of HAS on precipitated hydroxyapatite, J. Colloid Interface Sci. 69 (1979) 460–467.
[19] K.C. Dee, D.A. Puleo, R. Bizios, An Introduction to Tissue–Biomaterial Interactions, Wiley & Sons Inc., New Jersey, 2002, pp. 39–45.

[20] J. Garnett, P. Dieppe, The effects of serum and human albumin on calcium hydroxyapatite crystal growth, Biochem. J. 266 (1990) 863–868.
[21] K. Kandori, S. Sawai, Y. Yamamoto, H. Saito, T. Ishikawa, Adsorption of albumin on calcium hydroxyapatite, Colloids Surf., A Physicochem. Eng. Asp. 68 (1992) 283–289.
[22] D.T. Hughes Wassell, R.C. Hall, G. Embery, Adsorption of BSA onto hydroxyapatite, Biomaterials 16 (1995) 697–702.
[23] S.T. Manson, The calculation of photoionization cross sections: an atomic view, in Topics in Applied Physics, vol. 26, Springer-Verlag, New York, 1978, pp. 135–163.